IMPROVED SOLA INVERSIONS OF MDI DATA

R.M. Larsen[1], J. Christensen-Dalsgaard[2,3], A.G. Kosovichev[4], J. Schou[4]

[1]Datalogisk Institut, Aarhus Universitet, DK-8000 Århus C, Denmark
[2]Institut for Fysik og Astronomy, Aarhus Universitet, DK-8000 Århus C, Denmark
[3]Teoretisk Astrofysik Center, Danmarks Grundforskningsfond, Denmark
[4]W.W. Hansen Experimental Physics Laboratory, Stanford University, Stanford, CA 94305-4085, U.S.A.

ABSTRACT

We invert rotational splitting data (up to degree 250) from one year of SOI-MDI data, using the SOLA inversion method. We present an improved version of SOLA, where the target functions have been modified to match the behavior of the kernels for rotational splitting coefficients near the rotation axis. A test of the robustness of the improved method is carried out by inverting artificial data from the MDI Hare and Hounds exercise. This shows that these modifications improve the effective resolution near the pole, which allows us to assess more reliably the nature of the high-latitude features seen with other inversion methods. We analyze the averaging kernels and the error correlation between different points in the solution, the latter being a potential source of spurious features in the solutions.

Key words: Helioseismic inversion; SOLA method; solar rotation

1. INTRODUCTION

Inversions of the frequency splittings derived from the first 144 days of the MDI Medium-l program for the solar rotation rate have been performed using a variety of inversion techniques, as reported by Schou et al. (1998a). The different inversions were generally consistent with respect to the inferred rotation in the convection zone at latitudes below 70°; on the other hand, perhaps the most interesting feature, namely a prograde jet-like feature at 0.95 R, 75° latitude, was not unambiguously shown by all the inversions. Here we attempt to improve the performance of the SOLA technique, with regard to the reliability of the inversions at high latitudes, to allow a better assessment of the nature of the high-latitude features.

The MDI data are expressed in terms of splitting coefficients, a_j:

$$\Delta\nu_{nlm} = \nu_{nl} + \sum_{j=1}^{j_{\max}} a_j(n,l) P_j^{(l)}(m) \ ,$$

where $P_j^{(l)}$ are orthogonal polynomials in the azimuthal order m, of degree j. To first order, rotation only contributes to the odd splitting coefficients, which will be indexed by $j = 2s+1$.

We consider the SOLA technique (Pijpers & Thompson 1992, 1994; Larsen & Hansen 1997), which estimates the rotation rate at a given target location (r_0, θ_0), by forming linear combinations

$$\begin{aligned}\bar\Omega(r_0,\theta_0) &\equiv \sum_{i=1}^{M} c_i(r_0,\theta_0)\, a_i \\ &= \sum_{i=1}^{M} c_i(r_0,\theta_0) \int_0^{\pi/2}\int_0^R K_i(r,\theta)\,\Omega(r,\theta)\, r\mathrm{d}r\mathrm{d}\theta \\ &+ \sum_{i=1}^{M} c_i(r_0,\theta_0)\,\epsilon_i \ ,\end{aligned}$$

where i enumerates the odd a coefficients $a_{2s+1}(n,l)$, the K_i are the kernels relating the angular velocity Ω to a_i, and ϵ_i is the error in a_i. The coefficients $c_i(r_0,\theta_0)$ are chosen such that the *averaging kernel*

$$\mathcal{K}(r_0,\theta_0,r,\theta) = \sum_{i=1}^{M} c_i(r_0,\theta_0)\, K_i(r,\theta)$$

is localized near $r = r_0$, $\theta = \theta_0$, while the variance

$$\sigma[\Omega(r_0,\theta_0)]^2 = \sum_{i,j} c_i(r_0,\theta_0)\, E_{ij}\, c_j(r_0,\theta_0)$$

is constrained; here E_{ij} is the covariance matrix of the a_i, often assumed to be diagonal, $E_{ij} = \sigma_i^2\delta_{ij}$. To achieve the localization, $\mathcal{K}$ is approximated to a prescribed target $\mathcal{T}(r_0,\theta_0,r,\theta)$, by minimizing

$$\int_0^R\int_0^{\pi/2} [\mathcal{T}(r_0,\theta_0,r,\theta) - \mathcal{K}(r_0,\theta_0,r,\theta)]^2\, r\mathrm{d}r\mathrm{d}\theta + \lambda^2 \sum_{i,j} c_i\, E_{ij}\, c_j \ . \tag{1}$$

Here the first term ensures that the averaging kernel is close to the target, while the second controls the error in the inferred solution. The original version

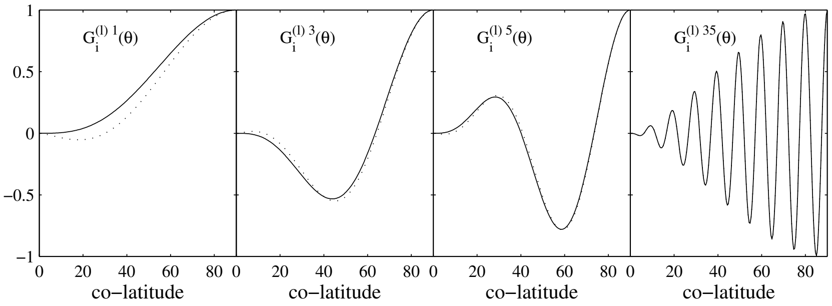

Figure 1. Plots of $G_i^{(l)2s+1}$ *for* $s = 0, 1, 2$ *and* 17 *(solid) and asymptotic expansions (dotted). Functions have been scaled to unity at colatitude* $90°$.

of the technique employed Gaussian targets, symmetrized around the equator. The radial width was chosen proportional to the sound speed (e.g. Thompson 1993), characterized by the value Δ_r at $r = 0.7R$, while the width Δ_θ in latitude had a constant linear extent. We use the efficient implementation of SOLA described by Larsen (1997).

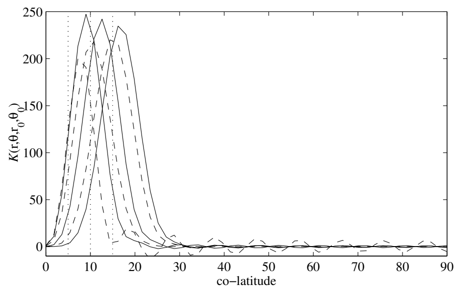

Figure 2. Cuts through averaging kernels at $r = 0.95R$ *for target locations* $(r_0, \theta_0) = (0.95R, 75°)$, $(0.95R, 80°)$ *and* $(0.95R, 85°)$, *with* $\Delta_\theta = 0.1$. *The dashed curves show the averaging kernels for Gaussian target functions, the solid curves the averaging kernels for Gaussian targets multiplied by* $\sin^{3/2}\theta$. *Vertical lines indicate the target locations.*

To test the various forms of the SOLA technique, we shall in the following use the `test2` dataset from the Hare and Hounds exercise described by Schou et al. (1998a). This dataset contains a coefficients generated from the artificial rotation law illustrated in Fig. 5a below. Gaussian noise with variance equal to that estimated for the real MDI data has been added.

The results of using the original implementation are shown in Fig. 5b. This implementation gives rise to several problems, which are mainly related to the latitudinal part of the inversion. Inversions with the target located close to the rotation axis result in averaging kernels with large sidelobes extending in latitude all the way to the equator. Also, reducing the latitudinal width of the target function below a certain point results in strong oscillations in both the averaging kernels and the inferred solution as a function of latitude. Finally, near the rotation axis, the averaging kernels are shifted away from their target positions towards lower latitudes. In the following we discuss these problems in more detail, based on an analysis of the properties of the kernels, and propose a way of reducing them.

2. MODIFIED TARGET FUNCTIONS

To understand the origin of these systematic errors, we note that the latitudinal behavior of the kernels K_i is given by functions $G_i^{(l)2s+1}$ on the form

$$G_i^{(l)2s+1} \equiv \gamma_i^{ls} \sin^2\theta \, P_{2s+1}^1(\cos\theta) \; , \quad i = 1, 2$$

(e.g. Pijpers 1997), where P_{2s+1}^1 is an associated Legendre polynomial and γ_i^{ls} is a normalization constant. Using an asymptotic expansion of the associated Legendre polynomials, we can write $G_i^{(l)2s+1}$ as

$$G_i^{(l)2s+1} \simeq \gamma'^{ls}_i \sin^{3/2}\theta \, \cos[(2s + 3/2)\theta + \pi/4] \; . \quad (2)$$

The functions $G_i^{(l)2s+1}$ and their expansions are shown in Fig. 1. It is evident that the asymptotic expression provides an excellent approximation to the latitude variation of the kernels, allowing simple analysis of the latitudinal properties of the inversion.

An obvious problem with the original SOLA method is that while $G_i^{(l)2s+1}$ goes to zero as $\sin^{3/2}\theta$ at the rotation axis, a Gaussian target function can be nonzero. A simple solution is to use as target a Gaussian multiplied by $\sin^{3/2}\theta$. The effect on the averaging kernels is illustrated in Fig. 2; here the dashed lines show the ringing at all latitudes which is induced by the use of the purely Gaussian target; as shown by the solid lines, this is almost completely removed by the scaling by $\sin^{3/2}\theta$. Also, the inversion at high latitudes is markedly improved (Fig. 5c).

The latitudinal properties of the inversion can now be analyzed by carrying out a 1D SOLA inversion in latitude with kernels $G_1^{(l)2s+1}$. Thus we determine inversion coefficients c_s that minimize

$$\int_0^{\pi/2} \left[\sum_{s=0}^{s_{\max}} G_1^{(l)2s+1}(\theta)\, c_s - \mathcal{T}(\theta, \theta_0) \right]^2 \mathrm{d}\theta$$
$$+ \lambda^2 \sum_{s=0}^{s_{\max}} \sigma_s^2 c_s^2 \; ,$$

where $\mathcal{T}(\theta, \theta_0)$ is the target function, which may be a Gaussian of width Δ_θ, or a Gaussian multiplied by $\sin^{3/2}\theta$, and for σ_s we have used error estimates of the splitting coefficients of the multiplet $l = 98$, $n = 1$ in the 144-d MDI dataset.

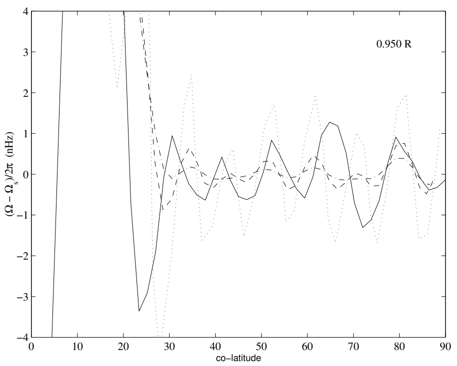

Figure 3. *Cuts at constant radius of* $0.95R$ *of SOLA inversions with different target width:* $\Delta_\theta = 0.05$ *(dotted),* 0.08 *(dashes) and* 0.1 *(dot-dashes); Gaussian targets multiplied by* $sin^{3/2}\theta$ *were used. The solution is plotted against the center of gravity of the averaging kernels. The solid line shows the rotation rate used to compute the artificial data. A three-term fit in* $\sin^2\theta$*, corresponding to the large-scale latitudinal variation, has been subtracted.*

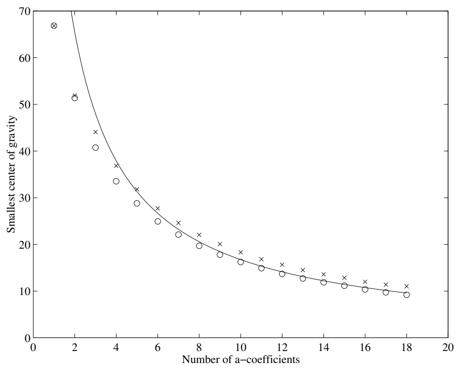

Figure 4. *Minimal colatitude at which an averaging kernel for a target of width* $\Delta_\theta = [\pi/(2s_{\max} + 3/2)]$ *can be localized, in 1D SOLA inversions in latitude for different number of* a *coefficients, with* λ *chosen to correspond to the regularization in the 2D inversion. Crosses correspond to a Gaussian, circles to a modified Gaussian target. The solid line shows* $\Delta_\theta/2$.

The 1D latitudinal description, including the inversion, offers a simple way of analyzing the properties of the full 2D problem. As an example, we note that ringing in the averaging kernels and solution can also result if the desired width of the averaging kernels is too small. To analyze this, we consider the case where Δ_θ small, such that $\sin^{3/2}\theta$ is almost constant over the interval $[\theta_0 - \Delta_\theta, \theta_0 + \Delta_\theta]$. Equation (2) shows that the SOLA inversion is essentially attempting to approximate $\mathcal{T}(\theta, \theta_0)$ by a sum of cosines. To avoid oscillations in the averaging kernels we must choose a target function with no significant Fourier components above the Nyquist frequency corresponding to the fastest oscillating cosine. This requires $\Delta_\theta > \pi/(2s_{\max} + 3/2)$. For the MDI data we have $s_{\max} = 17$ and hence Δ_θ should be larger than $\pi/35.5 \simeq 0.0885$. This may be compared with the 2D inversion results shown in Fig. 3, at various latitudinal target widths, indicating that a value of $\Delta_\theta \simeq 0.1$ is required to avoid oscillations in the solution, in reasonable agreement with the simple estimate.

The lower bound on the latitudinal width of the target also effectively determines how close to the rotation axis the SOLA method is capable of constructing well-localized averages. We have used the 1D latitudinal inversions to investigate this, choosing the trade-off parameter λ such as to correspond essentially to the 2D case, and with Δ_θ depending on $s_{\max}$ as discussed above. The results are shown in Fig. 4. The behavior is explained by the observation that by reducing θ_0 below approximately $\Delta_\theta/2$, oscillations start appearing in the averaging kernel, such that its center of gravity remains at this latitude.

3. LOCATION OF AVERAGING KERNELS AND REGION OF RELIABILITY

When the averaging kernels are shifted relative to the target, the inferred solution should be plotted against the actual location of the averaging kernel rather than the target location. The former can either be determined as the center of gravity $(r_{\rm cg}, \theta_{\rm cg})$,

$$r_{\rm cg} = \int_0^R \int_0^{\pi/2} r\, \mathcal{K}(r_0, \theta_0, r, \theta)\, r\, {\rm d}r{\rm d}\theta \ ,$$

$$\theta_{\rm cg} = \int_0^R \int_0^{\pi/2} \theta\, \mathcal{K}(r_0, \theta_0, r, \theta)\, r\, {\rm d}r{\rm d}\theta \ ,$$

or by fitting a Gaussian, symmetrized around the equator, to the averaging kernel. In general, the two methods give almost the same results; however, we tend to prefer the center of gravity, because the fitting often gives a misleading answer when the averaging kernel has a small peak sitting on a wide plateau, as might happen at high latitude. On the other hand, close to the equator the center of gravity is difficult to determine because of the symmetry of the averaging kernels around the equator; here the fit of a Gaussian is the preferred method to determine the location of the averaging kernel.

The locations of the centers of gravity essentially define the region over which inversion is possible. This may, for example, be used to analyze the extent to which the inversion can resolve features close to the rotation axis, depending on the number of a coefficients included (see also Fig. 4).

Since a large shift from the target position is often indicative of large sidelobes in the averaging kernels, we define the reliable part of the inversion as the set of points where $|r_{\rm cg} - r_{{\rm cg},0}|/\Delta_r < 0.2$ or $|\theta_{\rm cg} - \theta_{{\rm cg},0}|/\Delta_\theta < 0.2$. Here $(r_{{\rm cg},0}, \theta_{{\rm cg},0})$ is the center of gravity of the target function. In Fig. 5d the solution has been limited to the reliable region, so defined, and plotted against the center of gravity. It is evident that within the region shown, there is little difference between plotting against target location and against the center of gravity.

The ability of the solution to resolve the near-polar features is further illustrated in Fig. 6. With the original target functions (circles) the solution shows a spurious upturn close to the pole. This is suppressed by using the modified targets, which allows us to push the reliable region from 77° to about 82° at $0.95R$. More important is the removal of the systematic errors arising from non-local contributions to the

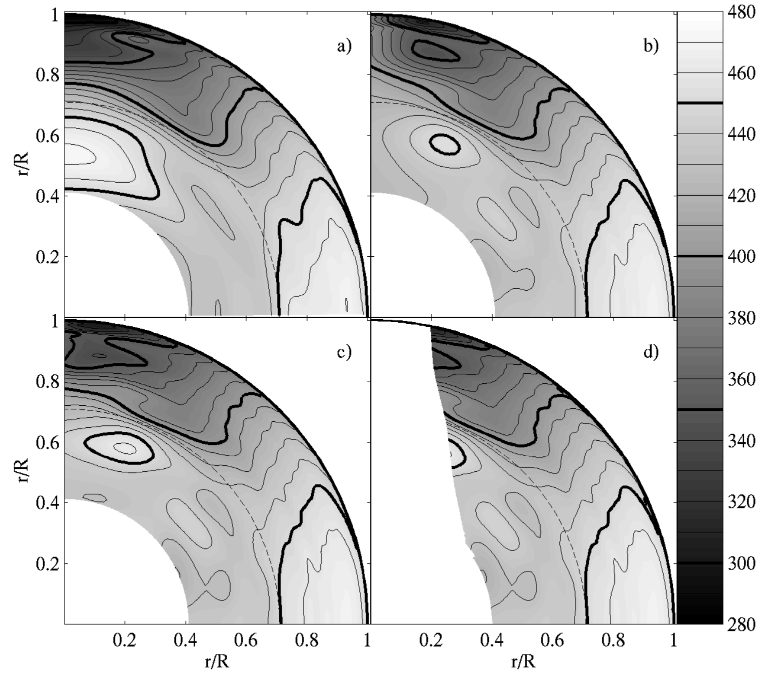

Figure 5. Artificial underlying rotation rate in the MDI Hare and Hounds dataset (panel a), and results of SOLA inversions of artificial data based on this rotation rate. Contours are in nHz. b) Original formulation, with Gaussian targets, plotted against the target location. c) Modified formulation, with Gaussian targets multiplied by $\sin^{3/2}\theta$*. d) As c), but plotted against the center of gravity of the averaging kernels and restricted to the reliable region.*

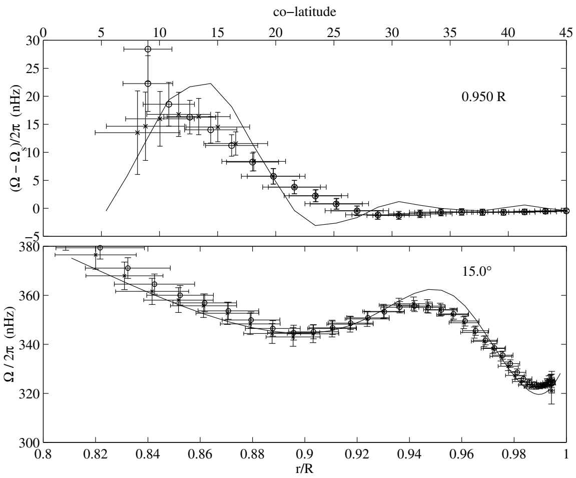

Figure 6. Cuts at constant radius (upper panel) and constant latitude (lower panel) of the inversions. The solid curve shows the assumed underlying rotation law, circles with error bars the original SOLA inversion with Gaussian targets and crosses with error bars the improved SOLA inversion, with Gaussian targets multiplied by $\sin^{3/2}\theta$*. The solutions have been plotted against the centers of gravity. The horizontal error bars show the inter-quartile distance of the averaging kernels. In the upper panel a three-term fit in* $\sin^2\theta$ *has been subtracted.*

inferred rotation rate. Also, the upper panel shows a beginning indication of the poleward downturn delimiting the jet in the artificial rotation curve. The resolution is somewhat better in radius than in latitude (cf. Fig. 7), and while the bump associated with the jet is smoothed out in latitude, it is reproduced quite well by the inversion in the radial direction, as shown in the lower panel of Fig. 6.

4. AVERAGING KERNELS AND ERROR CORRELATION FUNCTIONS

As pointed out by Howe & Thompson (1996) and Schou (1991), knowledge of the correlation between errors at different locations is important for interpreting features, such as the polar jet, in the solution. While the averaging kernel describes how the inferred solution is a smoothed representation of the true solution in the absence of noise, the error correlation function describes the extent to which errors propagated from the data to different points in the solution are correlated, and hence the width of the correlation function is indicative of the size of spurious features in the solution caused by noise. Howe & Thompson (1996) also demonstrated that in the one-dimensional case, a bad choice of the target parameters in the SOLA method can lead to large correlations between distant points.

Figure 7 shows the averaging kernels and the normalized error correlation function

$$C(r_1,\theta_1,r_2,\theta_2) = \frac{\sum c_i(r_1,\theta_1)c_i(r_2,\theta_2)}{\left[\sum c_i^2(r_1,\theta_1)\right]^{1/2}\left[\sum c_i^2(r_2,\theta_2)\right]^{1/2}} \,,$$

for the 2D SOLA inversion of the 144-d MDI dataset, with $(\Delta_r, \Delta_\theta) = (0.04, 0.1)$ and using the modified target functions described above. Since the inferred rotation rate represents an average weighted by the averaging kernel, one would expect errors in rotation estimates for points closer together than the width of the averaging kernels to be correlated, giving rise to a peak in the error correlation function of comparable width; this is indeed observed in 1D

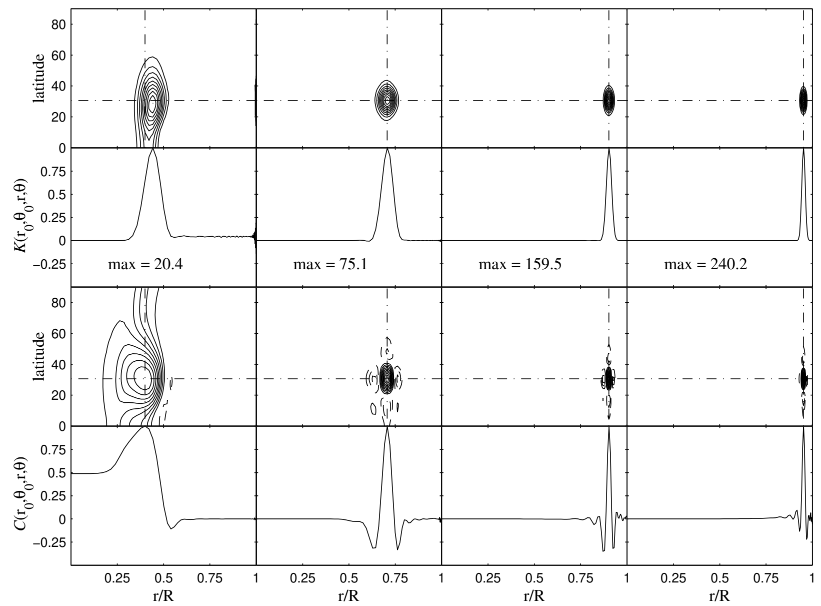

Figure 7. Averaging kernels and error-correlation function for the SOLA inversion, at target latitude $30.6°$*; columns 1 through 4 correspond to target radii* r_0 *of* $0.40R$, $0.707R$, $0.903R$ *and* $0.952R$*. In the contour plots, positive contours are solid and negative contours dashed; the dash-dotted lines indicate the target location* (r_0, θ_0)*. First row: averaging kernels, with contour spacings one tenth of the maximum value given in the second row. Second row: radial cuts through averaging kernels, at target latitude. Third row: Error correlation function* $C(r_0, \theta_0, r, \theta)$*, with contour spacing 0.1. Fourth row: radial cuts through error-correlation functions, at target latitude.*

inversions (e.g. Howe & Thompson 1996). Figure 7 shows that this is also the case for our SOLA inversions at locations above $\simeq 0.5R$. In the deep interior, however, the errors are highly correlated, since the solution here is determined by only a few deeply penetrating modes. At latitudes above 75° latitude $C(r_1, \theta_1, r_2, \theta_2)$ is somewhat spread out towards the rotation axis. This spread is a consequence of the averaging kernels drifting away from their target positions and would be eliminated if we plotted $C(r_1, \theta_1, r_2, \theta_2)$ against center of gravity of the averaging kernels, instead of target position. The well-localized error-correlation function in Fig. 7 gives us some confidence in our choice of target parameters.

Finally we should mention that we have tried to include estimates of the error correlation between a coefficients within the same multiplet (Schou et al. 1995, Gough 1996) in the inversion. The general effect is very small, with the largest difference between the solution with and without the error-correlation included being at the 1σ level. Also, the averaging kernels and error-correlation function for the solution remain almost unchanged.

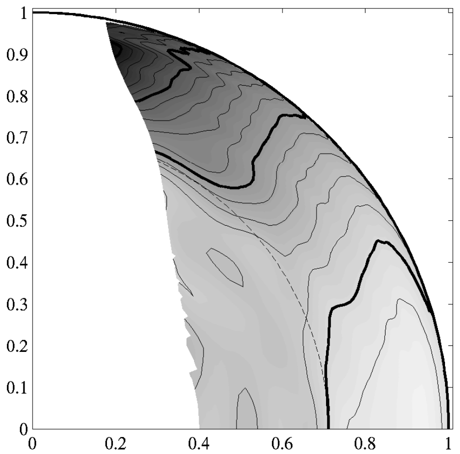

Figure 8. SOLA inversion, using modified targets, of the 144-d MDI data set. The solution has been restricted to the reliable region, and is plotted against the center of gravity. The grayscale coding is as in Fig. 5.

5. CONCLUSIONS

The modifications to the SOLA technique have clearly resulted in a significant improvement in the results, as tested on the artificial data (cf. Figs 5 and 6). In the reliable region the agreement with the true Hare and Hounds rotation rate is very good. It is likely that additional improvements can be made through further modifications of the target function, based also on analysis of the asymptotic approximation to the latitudinal variation of the kernels.

Figures 8 and 9 show the result of applying the improved SOLA to the 144-d MDI dataset. The general picture of the differential rotation in and just below the convection zone, the slowdown of the rotation at the pole and the structure of the tachocline agrees with the findings of Schou et al. (1998a) from the same dataset. However, we see no clear indication of a localized jet, but rather a ridge centered at $0.96R$ and extending between 65° and 80°. This feature is much less pronounced than the jet seen in the inversion of the artificial rotation profile, based on the RLS inversions of the 144-d MDI dataset. In particular, as seen in the upper panel of Fig. 9, the rotation rate decreases steadily towards the pole without any significant bump as seen in Fig. 6. Yet Howe et al. (1998) demonstrated beyond doubt that a high-latitude sig-

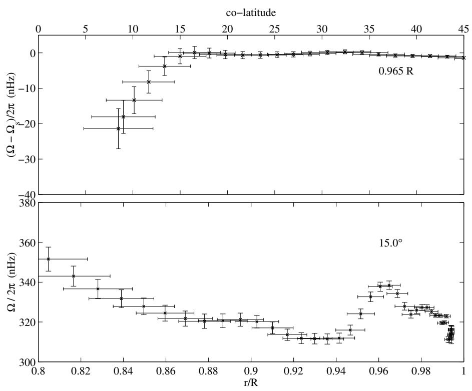

Figure 9. Cuts through the inversion of the 144-d MDI data set. In the upper panel a three-term fit in $\sin^2\theta$ *has been subtracted. Linestyles as in Fig. 6.*

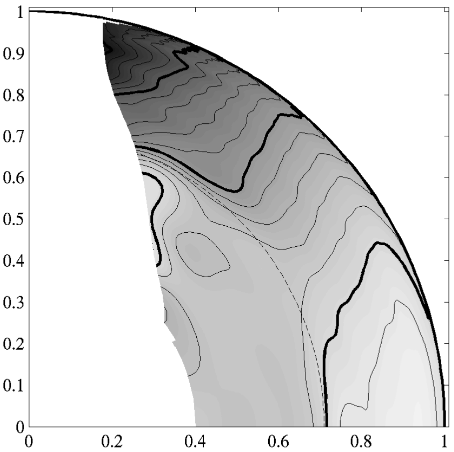

Figure 10. SOLA inversion, using modified targets, of the 360-d MDI data set. The solution has been restricted to the reliable region, and is plotted against the center of gravity. The grayscale coding is as in Fig. 5.

nal is present in the data.

Figures 10 and 11 show the result of applying the improved SOLA to a 360-d MDI dataset. These results look similar to those obtained for the 144-d dataset, except that the ridge is less pronounced. This should also be compared with the RLS-inversion of the 360-d MDI dataset (Schou et al. 1998b).

A possible explanation for the discrepancy between the RLS and SOLA inversions is the comparatively low latitudinal resolution of the SOLA method; thus, if the feature associated with the signal is very narrow, it might escape detection by SOLA. We note that the analysis of the error covariance function and our experiments with including error correlations for the data in the inversions give no reason for major concern in the SOLA inversions of MDI data. In any case, the properties of the high latitude feature, as well as the inversion methods still deserve further investigation (see also Howe et al. 1998).

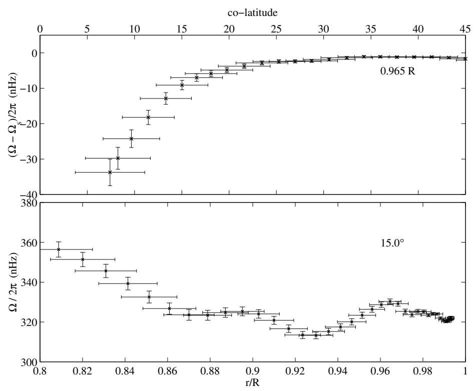

Figure 11. Cuts through the inversion of the 360-d MDI data set. In the upper panel a three-term fit in $\sin^2\theta$ *has been subtracted. Linestyles as in Fig. 6.*

ACKNOWLEDGEMENTS

The SOI–MDI project is supported by NASA grant NAG5-3077 to Stanford University. SOHO is a project of international cooperation between ESA and NASA. This work was partly supported by the Danish National Research Foundation through the establishment of the Theoretical Astrophysics Center.

REFERENCES

Gough, D. O., 1996, in: The structure of the Sun, ed. Roca Cortes, T., Cambridge University Press.

Howe, R., Antia, H., Basu, S., Christensen-Dalsgaard, J., Korzennik, S. G., Schou, J. & Thompson, M. J., 1998, these Proceedings.

Howe, R., Thompson, M. J., 1996, MNRAS, **281**, 1385.

Larsen, R. M., 1997, in: Proc. of the Interdisciplinary Inversion Workshop 5, ed. Jacobsen, B. H. (Århus: Dept. Earth Sciences, Aarhus University), 123.

Larsen, R. M., Hansen, P. C., 1997, A&AS, **121**, 587.

Pijpers, F. P., 1997, A&A, **326**, 1235.

Pijpers, F. P., Thompson, M. J., 1992, A&A, **262**, L33.

Pijpers, F. P., Thompson, M. J., 1994, A&A, **281**, 231.

Schou, J. 1991, in: Lecture Notes in Physics, Vol. 388, Challenges to Theories of the Structure of Moderate-Mass Stars, eds Gough, D. & Toomre, J. (Berlin: Springer Verlag), 93.

Schou, J., Christensen-Dalsgaard, J., Thompson, M. J., 1995, in: Proc. GONG'94: Helio- and Astro-seismology from Earth and Space, eds Ulrich, R. K., Rhodes, E. J., Jr, Däppen, W., PASPC, **76**, 528.

Schou, J., et al. 1998a, ApJ, **505**, in the press.

Schou, J., Christensen-Dalsgaard, J., Howe, R., Larsen, R. M., Thompson, M. J., Toomre, J., 1998b, these Proceedings.

Thompson, M. J., 1993, in: Proc. GONG 1992: Seismic Investigation of the Sun and stars, ed. Brown, T. M., PASPC, **42**, 141.